ARTICLE

Chinese Journal of Structural Chemistry

Construction of $ZnIn_2S_4$-$CdIn_2S_4$ Microspheres for Efficient Photo-catalytic Reduction of CO_2 with Visible Light

Shitong Han[1], Bifang Li[2], Lijuan Huang[2], Hailing Xi[1]*, Zhengxin Ding[2]* and Jinlin Long[2]*

[1]*State Key Laboratory of NBC Protection for Civilian, Beijing 102205, China*

[2]*State Key Laboratory of Photocatalysis on Energy and Environment, College of Chemistry, Fuzhou University, Fuzhou 3500116, China*

ABSTRACT $ZnIn_2S_4$ has emerged in water splitting and degradation of dyes due to its good stability and light absorption properties. However, there are still few reports of CO_2 photoreduction. Herein, we successfully synthesized $ZnIn_2S_4$ and obtained a series of $ZnIn_2S_4$-$CdIn_2S_4$ hetero-structured microspheres through the ion exchange method, and first used them in photocatalytic CO_2 reduction in noble-metal-free systems. The activity results showed that these $ZnIn_2S_4$-$CdIn_2S_4$ photocatalysts exhibit excellent catalytic activity under visible light, and the best CO yield is as high as 33.57 μmol·h^{-1} with a selectivity of 91%. Furthermore, the stability and reusability of $ZnIn_2S_4$-$CdIn_2S_4$ was firmly confirmed by diverse characterizations, including X-ray diffraction (XRD), scanning electron microscopy (SEM), transmission electron microscopy (TEM), X-ray photoelectron spectroscopy (XPS), energy-dispersive X-ray spectroscopy (EDX) and N_2 adsorption measurements.

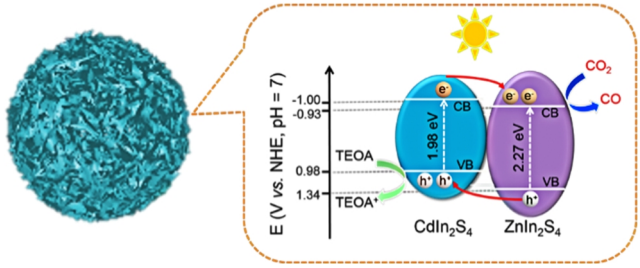

Keywords: CO_2RR, visible light photocatalysis, heterojunction, $CdIn_2S_4$

n INTRODUNTION

The excessive use of fossil fuels has led to a rapid increase in carbon dioxide emissions, which has caused a series of environmental problems such as the greenhouse effect.[1-3] Photocatalytic reduction CO_2 provides an attractive strategy to utilize carbon dioxide and realize carbon neutral energy cycle.[4-11] Unfortunately, due to the high thermodynamic stability of CO_2, fast recombination of photogenerated electron-holes and low selectivity of reaction, the photocatalytic performance is still unsatisfactory.[12-15]

Since the innovative demonstration of photoelectroncatalytic reduction of CO_2 using semiconductor powders by Inoue and coworkers[16] in 1979, a wealth of materials have been developed to catalyse CO_2 conversion reactions with light, both in homogeneous and heterogeneous systems. To date, semiconductor materials including TiO_2,[17,18] ZnO,[19,20] CeO_2,[21,22] Bi_2WO_6,[23,24] Ga_2O_3,[25-27] MOF[26] and CdS[28,29] have been reported as photocatalysts for CO_2 reduction. However, the poor efficiency of CO_2 photoreduction hinders its practical applications. Therefore, exploring and designing related photocatalytic reaction systems and suitable catalysts is the focus of current research.

Among various kinds of semiconductor photocatalysts, ternary sulfides of chalcogenide AB_2X_4 (*e.g.*, $ZnIn_2S_4$ and $CdIn_2S_4$) with unique physical and chemical properties, such as strong absorption in the visible region, excellent catalyst stability, appropriate band gaps and band edges, emerge in the field of photocatalysis.[30-33] Recently, there are many reports on the water splitting and dyes degradation of $ZnIn_2S_4$.[34,35] In regard of the field of photocatalytic CO_2 reduction, the performance of pure $ZnIn_2S_4$ material is still not satisfactory, mainly attributed to its low efficiency on separating photogenerated electron-hole pair.[36]

Owing to building the internal electric field, constructing heterojunctions between different semiconductors is an effective strategy to promote the separation of carriers, and thus enhance the activity and stability of photocatalysts.[37,38] As a convenient method to fabricate heterojunction, ion exchange not only makes the composition of inorganic nanocrystalline adjustable, but also maintains the morphology and structure of precursor.[39,40]

Herein, we design and synthesize $ZnIn_2S_4$-$CdIn_2S_4$ heterostructure through an in situ ion exchange strategy for CO_2 photoreduction under mild reaction conditions. The $ZnIn_2S_4$-$CdIn_2S_4$ composites are fully characterized by various physicochemical techniques (*e.g.*, XRD, SEM, TEM, EDX, XPS, DRS, and N_2 sorption measurement). Performance of the $ZnIn_2S_4$-$CdIn_2S_4$ catalyst is carried out in the classic CO_2 photoreduction system with $Co(bpy)_3^{2+}$ as a cocatalyst and triethanolamine (TEOA) as an electron donor. When evaluated as a visible light photocatalyst for CO_2 reduction, the optimized $ZnIn_2S_4$-$CdIn_2S_4$ heterostructure exhibits considerable activity and excellent stability for selectively reducing CO_2 into CO without the assistance of noble metal cocatalyst. The generation rate of CO is 33.57 μmol·h^{-1} under visible irradiation, mostly, with a highly selectivity of 91%. PL and transient photocurrent analyses indicate that the $ZnIn_2S_4$-$CdIn_2S_4$ catalyst can efficiently impede the recombination and promote the transfer of photoexcited charges.

n RESULTS AND DISCUSSION

Powder X-ray diffraction (XRD) is performed to study the crystal structures and phase purities of synthetic materials. As presented in Figure S1, the peaks at 3.58, 21.58, 27.96 and 47.18° are well indexed to the (001), (006), (102) and (110) crystal planes of $ZnIn_2S_4$ phase (JCPDS card no. 03-065-2023),[41] and no other noticeable peaks are witnessed, pointing to the high purity of the synthesized $ZnIn_2S_4$ material. All the peaks in $ZnIn_2S_4$-$CdIn_2S_4$-*x* (*x* = 15, 30, 45, 60) composites are matched well with $ZnIn_2S_4$, and no obvious $CdIn_2S_4$ peaks can be observed. This result can be attributed to the following two points. On one hand, the main diffraction peaks of $CdIn_2S_4$ are very similar to that of $ZnIn_2S_4$, and on the other hand, the $CdIn_2S_4$ is highly dispersed in the

DOI: 10.14102/j.cnki.0254-5861.2021-0026

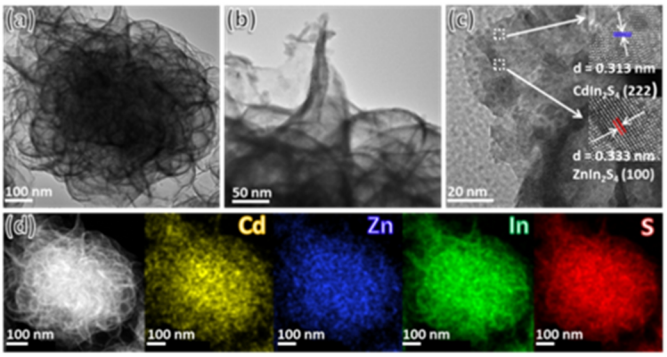

Figure 1. (a–b) TEM images, (c) HRTEM image, and (d) elemental mappings of $ZnIn_2S_4$-$CdIn_2S_4$ microspheres.

sample. Besides, in order to verify the ratio of $CdIn_2S_4$ in $ZnIn_2S_4$-$CdIn_2S_4$, we investigate the molar ratios of Zn and Cd in different samples using ICP-OES. As shown in Table S1, the content of Cd^{2+} increases with the longer hydrothermal time, which means that more $ZnIn_2S_4$ is replaced by $CdIn_2S_4$.

The morphology of the as-synthesized samples is investigated by SEM. As shown in Figure S2(a–b), the pure $ZnIn_2S_4$ exhibits microspheres composed of nanosheets with diameter of about 1 μm. When the hydrothermal ion exchange time increases from 15 to 60 min, according to Figure S2(c–f), the composite still retains original sphere appearance without significant change, which may be attributed to the low hydrothermal temperature and the highly stable structure of $ZnIn_2S_4$. TEM analysis is performed to further discriminate the morphology and structure of $ZnIn_2S_4$-$CdIn_2S_4$. In Figure 1a, the $ZnIn_2S_4$-$CdIn_2S_4$ shows apparent spherical structure, which is consistent with the SEM images. The nanosheets are clearly observed in higher magnification TEM image (Figure 1b). As indicated in Figure 1c, the lattice fringes with a spacing of 0.333 and 0.313 nm can be discerned, which represent the (100) crystal plane of $ZnIn_2S_4$ and the (222) crystal plane of $CdIn_2S_4$, respectively. Moreover, the elemental mapping images (Figure 1d) of $ZnIn_2S_4$-$CdIn_2S_4$ show that elements Cd, Zn, In and S are homogeneously distributed throughout the whole composite, and no other elements are present. Therefore, the above TEM analysis confirmed that $ZnIn_2S_4$-$CdIn_2S_4$ with 3D microsphere structure possesses heterojunction made up of $ZnIn_2S_4$ and $CdIn_2S_4$.

XPS analyses are carried out to study the surface chemical composition and electronic state of $ZnIn_2S_4$-$CdIn_2S_4$. The C 1*s* at 284.6 eV is used as a reference to correct the binding energy of other elements. The high resolution XPS spectrum of Cd 3*d* is depicted in Figure 2a, where two peaks positioned at the binding energies of 405.23 and 411.97 eV are correspondingly assigned to Cd $3d_{5/2}$ and Cd $3d_{3/2}$ with a spin-orbit coupling of 6.7 eV, which is in good accordance with the reported values in $CdIn_2S_4$ materials.[42] In the high-resolution XPS spectra of Zn 2*p*, two peaks located at 1021.79 and 1044.96 eV correspond to Zn $2p_{3/2}$ and Zn $2p_{1/2}$, respectively, suggesting the Zn element holds the valance state of +2.[43,44] In the In 3*d* core-level spectrum (Figure 2c), the peak splitting to In $3d_{5/2}$ and In $3d_{3/2}$ are at around 452.47 and 444.87 eV, respectively, which is characteristic of the In^{3+} cation.[45] The peaks at around 162.7 and 161.6 eV in S 2*p* high-resolution XPS spectrum represent S $2p_{3/2}$ and S $2p_{1/2}$, respectively, corresponding to S^{2-} species in the composite.[46] All results indicate the elements in $ZnIn_2S_4$-$CdIn_2S_4$ heterostructures

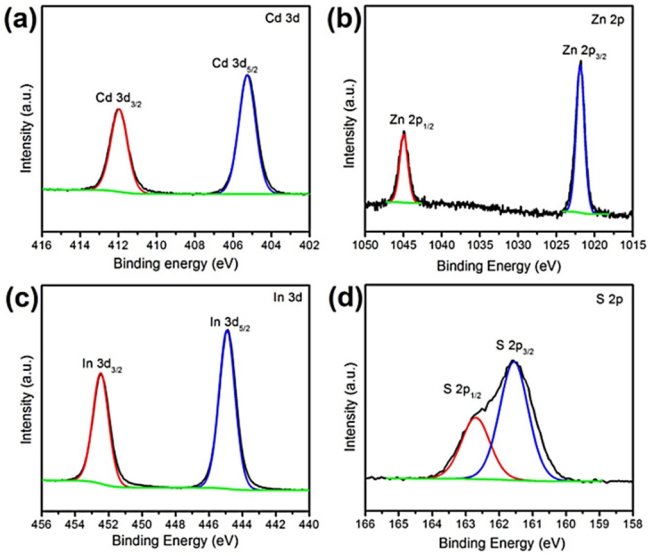

Figure 2. High-resolution XPS spectra of $ZnIn_2S_4$-$CdIn_2S_4$ microspheres: (a) Cd 3*d*, (b) Zn 2*p*, (c) In 3*d*, and (d) S 2*p*.

exist in chemical states of In^{3+}, Cd^{2+}, Zn^{2+} and S^{2-}.

The textural characteristics of $ZnIn_2S_4$-$CdIn_2S_4$ material are investigated by N_2 sorption measurements. As shown in Figure 3a, the N_2 adsorption-desorption isotherms of $ZnIn_2S_4$-$CdIn_2S_4$ manifests are categorized as the type IV fashion, a type H3 hysteresis loop, suggesting that the material possesses a mass of mesopores.[47,48] The specific BET surface area and pore volume of $ZnIn_2S_4$-$CdIn_2S_4$ are calculated to be 182 and 0.326 $cm^3 \cdot g^{-1}$, respectively. Meanwhile, the specific BET surface area of $ZnIn_2S_4$ is 159 $m^2 \cdot g^{-1}$, which is much smaller than that of $ZnIn_2S_4$-$CdIn_2S_4$. As shown in Figure 3a (inset), the pore size of the sample is at the range of 5–20 nm, confirming the existence of mesoporous in $ZnIn_2S_4$-$CdIn_2S_4$. Furthermore, CO_2 adsorption-desorption measurements are conducted to investigate the CO_2 adsorption of materials. As is shown in Figure 3b, $ZnIn_2S_4$-$CdIn_2S_4$ composite exhibits a CO_2 adsorption capacity of 12.9 $cm^3 \cdot g^{-1}$ under the condition of 0 °C and 1 atm, which is slightly higher than that of pure $ZnIn_2S_4$ (11.8 $cm^3 \cdot g^{-1}$). In general, the high surface area, pore volume and CO_2 absorbance of sample are favourable to provide more catalytic active sites, promote charge transportation, and facilitate CO_2 capture/adsorption, thus contributing to the improvement of photocatalytic activity. In order to verify the difference in activation ability over CO_2 between the two samples, we have conducted linear sweep voltammetry (LSV) measurement of $ZnIn_2S_4$ and $ZnIn_2S_4$-$CdIn_2S_4$ as working electrode in CO_2 atmosphere. As shown in Figure 3c, $ZnIn_2S_4$-$CdIn_2S_4$ possesses a more positive initial potential and a higher current density than pure $ZnIn_2S_4$, implying that the $ZnIn_2S_4$-$CdIn_2S_4$ can effectively activate CO_2.

Optical absorption characteristics of the synthesized samples are determined by UV-Vis diffuse reflectance spectroscopy (DRS) measurements. As displayed in Figure S3a, there is an obvious red shift with the introduction of $CdIn_2S_4$, compared with $ZnIn_2S_4$. It is anticipated that $ZnIn_2S_4$-$CdIn_2S_4$ can absorb more visible light for photoexcitation of electron-hole charge carriers. From the Tauc plots (Figure S3b), the band energies of $ZnIn_2S_4$ and $ZnIn_2S_4$-$CdIn_2S_4$ are calculated to be 2.27 and 2.14 eV,[49,50] respectively, suggesting the increase of visible light absorption of

DOI: 10.14102/j.cnki.0254-5861.2021-0026

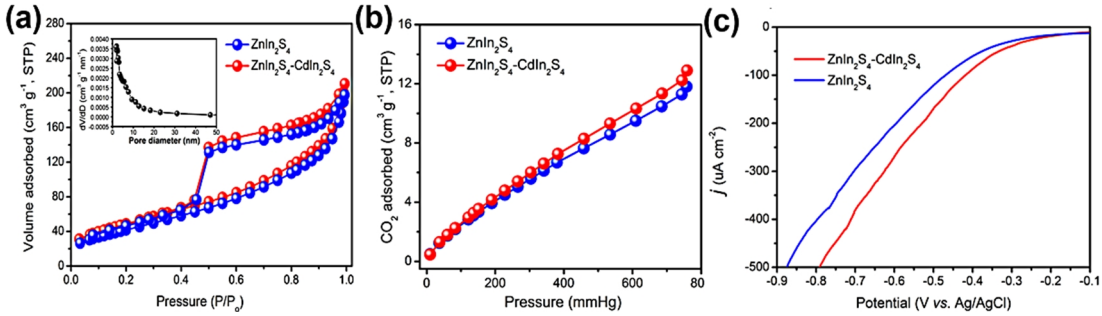

Figure 3. (a) N_2 adsorption-desorption isotherms (inset is the corresponding pore-size distribution plot of $ZnIn_2S_4$-$CdIn_2S_4$), (b) CO_2 adsorption isotherms and (c) LSV curves of $ZnIn_2S_4$ and $ZnIn_2S_4$-$CdIn_2S_4$.

$ZnIn_2S_4$-$CdIn_2S_4$. The result is in faithful agreement with the trend in photocatalytic performances discussed later.

The CO_2 photoreduction performance of the $ZnIn_2S_4$-$CdIn_2S_4$ is investigated in the tandem catalytic system under mild conditions (*i.e.*, 1 atm CO_2 and 30 °C) by employing $Co(bpy)_3^{2+}$ (bpy = 2,2′-bipyridine), as cocatalyst, electron donor and solvent, respectively.[51] Figure 4a depicts the CO and H_2 production rate of different samples. CO is detected as the sole CO_2 reduction product, coupled with a small amount of H_2, which is in agreement with the results of previous works.[52] The pure $ZnIn_2S_4$ only exhibited CO generation rate of 13.5 μmol, mainly due to the high recombination rate of photogenerated electronhole pairs. However, with the addition of Cd^{2+} to form $CdIn_2S_4$, the activity of CO_2 photoreduction is improved. In particular, $ZnIn_2S_4$-$CdIn_2S_4$-30 composite exhibits a high product selection rate of 91%, generating 33.6 μmol CO, which is almost twice more than that of pure

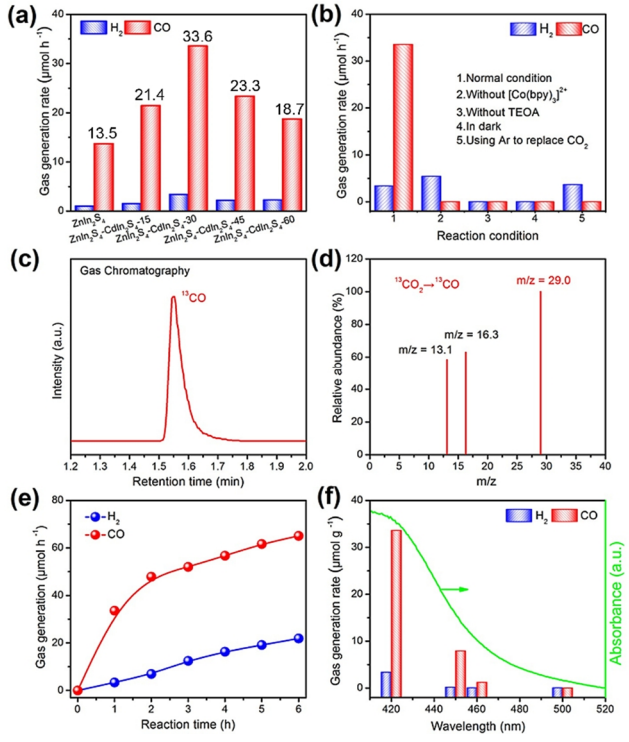

Figure 4. (a) CO_2 photoreduction activities of different samples, (b) CO_2 reduction performance under various conditions, gas chromatography (c) and mass spectra analysis (d) of CO generated from the $^{13}CO_2$ isotope experiment. (e) Time-yield plots of products, and (f) CO/H_2 production under light irradiation of different wavelengths.

$ZnIn_2S_4$. Besides, the apparent quantum efficiency (AQE) of CO production is calculated to be 0.59%. The photocatalytic CO_2-to-CO reduction efficiency of $ZnIn_2S_4$-$CdIn_2S_4$ material is comparable to that of other reported works in similar system.[30,49,53-56] Nevertheless, when the hydrothermal reaction time is extended to 45 or 60 min, the introduction of excessive $CdIn_2S_4$ reduces the activity of the composites. The outstanding CO_2 reduction performance of the $ZnIn_2S_4$-$CdIn_2S_4$ photocatalyst should be mainly ascribed to the heterostructure between $ZnIn_2S_4$ and $CdIn_2S_4$, which can not only provide larger surface area and abundant active sites for CO_2 adsorption and surface redox catalysis, but also promote the separation and migration of photo-induced charge carriers.

Furthermore, a series of control experiments are performed to demonstrate the functions of CO_2 photoreduction system (Figure 4b). Fewer CO is produced without the presence of $[Co(bpy)_3]^{2+}$ (Figure 4b, column 2), indicating that $[Co(bpy)_3]^{2+}$ can remarkably enhance the photocatalytic activity of pristine semiconductor photocatalysts for heterogeneous CO_2 conversion.[57] No CO and H_2 are produced in the absence of TEOA (Figure 4b, column 3), suggesting that sacrificial agent can inhibit the reverse reaction, thus promoting the CO_2 photo-reduction reaction. No gas products are detected under dark condition (Figure 4b, column 4), implying the photocatalytic nature of the reaction. In addition, when Ar is employed as the gas source, H_2 is the only gaseous product in the reaction system (Figure 4b, column 5), which indicates that CO originates from the CO_2. To get deep insights into the carbon source of produced CO, we conducted ^{13}C-labelled isotropic experiment under the identical photo-reaction conditions. As shown in Figure 4(c–d), the peak with the m/z value of 29 in the results of GC-MS analysis is assigned to ^{13}CO. This test powerfully verifies that the generated CO stems from the CO_2 rather than from other organic substances in the hybrid chemical system.[58]

The time-yield plots of the products are illustrated in Figure 4e. As revealed, the production of CO_2 increases roughly linearly in the first two hours. However, the reaction rate slows down for the next few hours as the concentration of reactants decreases. After photoreduction for six hours, the overall yield of CO_2 reaches 65 μmol. The catalytic activity of $ZnIn_2S_4$-$CdIn_2S_4$ for CO_2 photoreduction is further studied under different illumination wavelengths. As shown in Figure 4f, the tendency of gas evolution is in good agreement with the optical absorption spectrum of the $ZnIn_2S_4$-$CdIn_2S_4$-30 material. This observation reveals CO_2 reduction reaction is triggered by photoexcitation of the $ZnIn_2S_4$-$CdIn_2S_4$-30 catalyst to achieve charge generation, separation and subsequ-

DOI: 10.14102/j.cnki.0254-5861.2021-0026

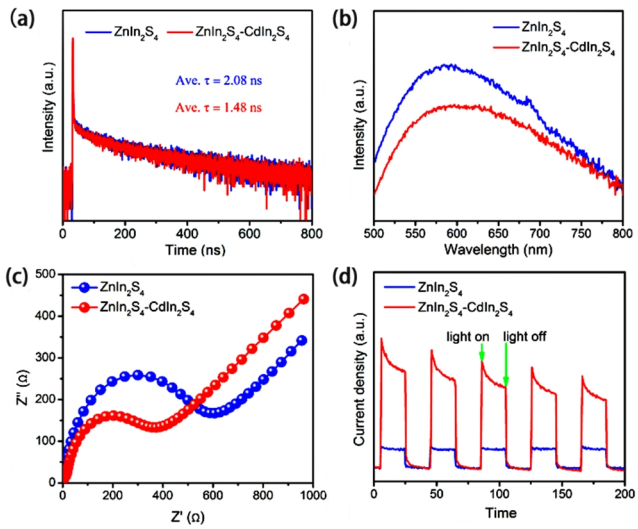

Figure 5. (a) Time-resolved transient PL decay, (b) Steady-state PL spectra under excitation wavelength of 468 nm, (c) EIS spectra, and (d) transient photocurrent spectra of $ZnIn_2S_4$-$CdIn_2S_4$ and $ZnIn_2S_4$.

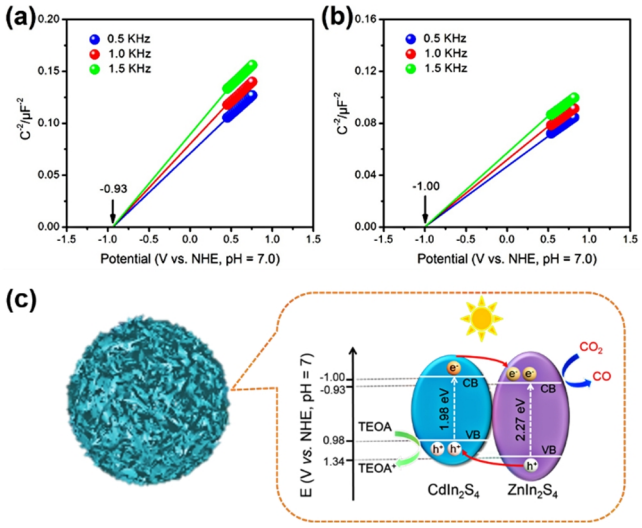

Figure 6. Mott-Schottky plots of (a) $ZnIn_2S_4$ and (b) $CdIn_2S_4$. (c) Proposed CO_2 photoreduction mechanism over $ZnIn_2S_4$-$CdIn_2S_4$ microspheres.

ent tandem electron transfer catalysis.[59,60]

We also examine the stability and reusability of $ZnIn_2S_4$-$CdIn_2S_4$, which are highly important for its advanced development. After photocatalytic experiments, the $ZnIn_2S_4$-$CdIn_2S_4$ is separated from the reaction mixture, washed with ethanol, and dried in air. The used sample is employed for later photocatalytic CO_2 reduction operations. As presented in Figure S4a, in the third recycle some deactivation was observed, but thereafter the $ZnIn_2S_4$-$CdIn_2S_4$ solid exhibits brilliant activity stability, disclosing its high reusability for the CO_2 photo-fixation reaction. XRD is carried out to further confirm the stability of the catalyst. As indicated in Figure S4b, compared with the fresh $ZnIn_2S_4$-$CdIn_2S_4$ material, the diffraction peaks of the used sample are almost unchanged. The results also suggest the high structural stability of catalyst.

Photoelectrochemical characterizations are performed to elucidate the high CO_2 reduction performance of $ZnIn_2S_4$-$CdIn_2S_4$ heterojunction photocatalyst. First, the specific charge carrier dynamics of $ZnIn_2S_4$ and $ZnIn_2S_4$-$CdIn_2S_4$ particles are probed by time-resolved photoluminescence (PL) spectroscopy (Figure 5a). After compositing with $CdIn_2S_4$, the average emission lifetime of $ZnIn_2S_4$-$CdIn_2S_4$ is longer, indicating that $ZnIn_2S_4$-$CdIn_2S_4$ can provide more photo-induced carriers in the photocatalytic reduction process.[61] As revealed in Figure 5b, a clear PL quenching is detected for the $ZnIn_2S_4$-$CdIn_2S_4$ sample compared with pare $ZnIn_2S_4$, proving that the recombination rate of photoinduced charge carriers is prohibited.[62] Meanwhile, we carried out electrochemical impedance spectra (EIS), as shown in Figure 5c. $ZnIn_2S_4$-$CdIn_2S_4$ manifests a smaller semicircle, suggesting a lower charge-transfer resistance in the heterostructures, which permits the fast transport and separation of photoinduced charges.[63,64] Moreover, the transient photocurrent spectra demonstrate that $ZnIn_2S_4$-$CdIn_2S_4$ can deliver an evidently strengthened photocurrent response compared with the naked $ZnIn_2S_4$ (Figure 5d), revealing the enhanced transfer of charge carriers in the composite.[65,66] The above results suggest that the $ZnIn_2S_4$-$CdIn_2S_4$ hierarchical can facilitate the separation and transport of photoinduced charges, thus accordingly improving the CO_2 photoreduction performance.

By combining the results of bandgaps and Mott-Schottky curves (Figure 6a, b), the conduction band (CB) and valence band (VB) positions of $ZnIn_2S_4$ and $CdIn_2S_4$ are calculated to be −0.93, 1.34, −1.00 and 0.98 V (*vs.* normal hydrogen electrode, NHE, pH = 7), respectively.[67,68] Hence, the redox potentials of $ZnIn_2S_4$-$CdIn_2S_4$ composite are suitable for CO_2 photo-reduction reaction. The possible photocatalytic CO_2 reduction process over $ZnIn_2S_4$-$CdIn_2S_4$ is depicted in Figure 6c. When exposed to visible light, $ZnIn_2S_4$ and $CdIn_2S_4$ semiconductors can be excited to give off electrons in CB, remaining holes in VB, respectively. Owing to the favorable heterojunction and intimate interfacial contact between $ZnIn_2S_4$ and $CdIn_2S_4$, the generated electrons can easily transfer from the $CdIn_2S_4$ to $ZnIn_2S_4$, and then further reduce the adsorbed CO_2 to produce CO.[55,69] In the meantime, the holes accumulated in the VB of $CdIn_2S_4$ are consumed by TEOA, and the whole redox reaction of the photocatalytic system is thus completed.

n CONCLUSION

In summary, the $ZnIn_2S_4$-$CdIn_2S_4$ heterostructures with flake microspheres are synthesized using a simple ion exchange method for efficient reduction CO_2 in visible light. After combining with $CdIn_2S_4$, $ZnIn_2S_4$-$CdIn_2S_4$ exhibits large surface area, preferable light absorption, and accelerated separation of photoexcited charges tested by a series of instruments. Therefore, $ZnIn_2S_4$-$CdIn_2S_4$ hybrid exhibits considerable performance for CO_2 deoxygenation with a high CO evolution rate of 33.57 μmol·h^{-1} and selection rate of 91%. This work may encourage further studies on the design and construction of complex semiconductor-based photocatalysts for photocatalytic CO_2 reduction toward the sustained solar fuel generation.

n EXPERIMENTAL

Synthesis of Materials. All reagents were obtained from commercial sources and used without further purification.

Synthesis of $ZnIn_2S_4$. 15.2 mg $Zn(Ac)_2·2H_2O$, 48 mg

DOI: 10.14102/j.cnki.0254-5861.2021-0026

$In(NO_3)_3·XH_2O$ and 64 mg L-cysteine hydrochloride were dissolved in 15 mL ethanol and 5 mL glycol with magnetically stirring for 30 min. Then, the homogeneous solution was transferred into a 25 mL Teflon-lined stainless-steel autoclave and maintained at 160 ℃ for 5 h in an electric oven. After the temperature was cooled to room temperature, the precipitate was collected, washed and dried, yielding the yellow $ZnIn_2S_4$ product.

Synthesis of $ZnIn_2S_4$-$CdIn_2S_4$. Conversion of $ZnIn_2S_4$ to $ZnIn_2S_4$-$CdIn_2S_4$ was realized *via* an efficient cation exchange method. The $ZnIn_2S_4$ was dispersed in 9 mL ultrapure water, followed by the addition of 1 mL of $CdCl_2$ solution (0.1 M). The resultant mixture was stirred for 30 min and then maintained at 120 °C for 15, 30, 45 and 60 min, respectively. Afterwards, the obtained yellow-green precipitates were filtrated, washed with H_2O and ethanol, dried overnight in an oven at 60 °C. The products obtained were designated as $ZnIn_2S_4$-$CdIn_2S_4$-15, $ZnIn_2S_4$-$CdIn_2S_4$-30, $ZnIn_2S_4$-$CdIn_2S_4$-45 and $ZnIn_2S_4$-$CdIn_2S_4$-60, respectively.

Synthesis of $CdIn_2S_4$. In a typical process, the precursor solutions of $Cd(NO_3)_2·4H_2O$, $In(NO_3)_3·4H_2O$, and thioacetamide (TAA) with the molar ratio of 1:2:4 were dissolved in ethylene glycol, followed by stirring for 40 min using magnetic stirrer. The obtained homogeneous phase solution was transferred into a 100 mL Teflon-lined stainless-steel autoclave and maintained at 160 °C for 12 h. After the reaction was completed, the autoclave was naturally cooled to room temperature. The resulting precipitates were fully purified and rinsed six times with ethanol and deionized water, and then dried in air at 60 °C for 8 h.

Characterization of Materials. The crystal phases of the samples were analyzed by X-ray diffraction (XRD) on a Bruker D8 Advance instrument (CuKα irradiation, λ = 1.5406 Å). The morphology and structure of the samples were examined by field emission scanning electron microscope (FESEM; JEOL-6700) and transmission electron microscope (TEM; JEOL, JEM-2010). The TEM instrument was employed to capture elemental mapping images and X-ray spectroscope (EDX). N_2 and CO_2 adsorption isotherms were collected on an ASAP2020M apparatus. The samples were degassed in vacuum at 100 °C for 6 h, and then measured at 77 and 273 K to determine N_2 and CO_2 adsorption, respectively. UV-vis diffuse reflectance spectra (DRS) were obtained on a Varian Cary 500 UV-Vis-NIR spectrophotometer with $BaSO_4$ as a reflectance standard. X-ray photo-electron spectroscopy (XPS) was carried out on a PHI Quantum 2000 XPS system with C 1*s* binding energy (284.6 eV) as the reference and He I excitation energy (21.22 eV) as the monochromatic light source. Photoluminescence (PL) characterizations were carried out on a Hitachi F-7000 spectrophotometer at room temperature. The electrochemical analysis was carried out on CHI600E Electrochemical System, using a conventional three-electrode cell with Pt plate and Ag/AgCl electrode as the counter and reference electrodes, respectively. An Agilent 7890B gas chromatograph (GC) equipped with a thermal conductivity detector (TCD) and a packed column (TDX-01) was utilized to analyze and quantify the gases produced from the CO_2 photoreduction system using Ar as the carrier gas. An HP 5973 gas chromatography-mass spectrometer (GC-MS) was employed to analyze the gaseous products generated from the $^{13}CO_2$ (97% enriched) isotopic experiment and to determine whether other potential products were generated in the liquid phase.

Photocatalytic CO_2 Reduction Testing. In the typical photocatalytic CO_2 reduction reaction, 4 mg of photocatalysts, 200 μmol of bipyridine (bpy), 4 μmol of $CoCl_2$, 2 mL of triethanolamine (TEOA), 2 mL of H_2O and 8 mL of acetonitrile (MeCN) were added into a 160 mL reactor. Then, high purity CO_2 was introduced into the reactor with a partial pressure of 1 atm. A 300W Xe lamp with a 420 nm cutoff filter was used as the light source. The temperature of the reaction system was kept at 30 °C. During photocatalytic process, the reaction system was vigorously stirred with a magnetic stirrer. After reaction, the generated products were quantified by an Agilent 7890B gas chromatograph.

n ACKNOWLEDGEMENTS

This work is supported by National Natural Science Foundation of China (FZUL 21876204 and 22072022) and the State Key Laboratory of NBC Protection (SKLNBC2019-14 and SKLNBC2020-18).

n AUTHOR INFORMATION

Corresponding authors. Email: fhxihl@163.com, zxding@fzu.edu.cn, jllong@fzu.edu.cn

n COMPETING INTERESTS

The authors declare no competing interests.

n ADDITIONAL INFORMATION

Supplementary information is available for this paper at http://manu30.magtech.com.cn/jghx/EN/10.14102/j.cnki.0254-5861.2021-0026

For submission: https://mc03.manuscriptcentral.com/cjsc

REFERENCES

(1) Armstrong, R. C.; Wolfram, C.; De Jong, K. P.; Gross, R.; Lewis, N. S.; Boardman, B.; Ragauskas, A. J.; Ehrhardt-Martinez, K.; Crabtree, G.; Ramana, M. V. The frontiers of energy. *Nat. Energy* **2016**, 1, 15020.

(2) Fu, J.; Jiang, K.; Qiu, X.; Yu, J.; Liu, M. Product selectivity of photocatalytic CO_2 reduction reactions. *Mater. Today* **2020**, 32, 222–243.

(3) Li, X.; Yu, J.; Jaroniec, M.; Chen, X. Cocatalysts for selective photoreduction of CO_2 into solar fuels. *Chem. Rev.* **2019**, 119, 3962–4179.

(4) Rao, H.; Schmidt, L. C.; Bonin, J.; Robert, M. Visible-light-driven methane formation from CO_2 with a molecular iron catalyst. *Nature* **2017**, 548, 74–77.

(5) Chang, X.; Wang, T.; Yang, P.; Zhang, G.; Gong, J. The development of cocatalysts for photoelectrochemical CO_2 reduction. *Adv. Mater.* **2019**, 31, 1804710.

(6) Tu, W.; Zhou, Y.; Zou, Z. Photocatalytic conversion of CO_2 into renewable hydrocarbon fuels: state-of-the-art accomplishment, challenges, and prospects. *Adv. Mater.* **2014**, 26, 4607–4626.

(7) White, J. L.; Baruch, M. F.; Pander, J. E.; Hu, Y.; Fortmeyer, I. C.; Park, J. E.; Zhang, T.; Liao, K.; Gu, J.; Yan, Y.; Shaw, T. W.; Abelev, E.; Bocarsly, A. B. Light-driven heterogeneous reduction of carbon dioxide: photocatalysts and photoelectrodes. *Chem. Rev.* **2015**, 115, 12888–12935.

(8) Zhang, P.; Wang, S.; Guan, B. Y.; Lou, X. W. Fabrication of CdS hierarchical multi-cavity hollow particles for efficient visible light CO_2

DOI: 10.14102/j.cnki.0254-5861.2021-0026

reduction. *Energy Environ. Sci.* **2019**, 12, 164–168.

(9) Xia, Y.; Yu, J. Reaction: rational design of highly active photocatalysts for CO_2 conversion. *Chem* **2020**, 6, 1039–1040.

(10) Liu, S.; Li, Y.; Ding, K.; Chen, W.; Zhang, Y.; Lin, W. Mechanism on carbon vacancies in polymeric carbon nitride for CO_2 photoreduction. *Chin. J. Struct. Chem.* **2020**, 39, 2068–2076.

(11) Cheng, L.; Zhang, D. N.; Liao, Y. L.; Fan, J. J.; Xiang, Q. J. Structural engineering of 3D hierarchical $Cd_{0.8}Zn_{0.2}S$ for selective photocatalytic CO_2 reduction. *Chin. J. Catal.* **2021**, 42, 131–140.

(12) Ran, J.; Jaroniec, M.; Qiao, S. Cocatalysts in semiconductor-based photocatalytic CO_2 reduction: achievements, challenges, and opportunities. *Adv. Mater.* **2018**, 30, 1704649.

(13) Wang, S.; Guan, B. Y.; Lou, X. W. Rationally designed hierarchical N-doped carbon@$NiCo_2O_4$ double-shelled nanoboxes for enhanced visible light CO_2 reduction. *Energy Environ. Sci.* **2018**, 11, 306–310.

(14) Sakakura, T.; Choi, J. C.; Yasuda, H. Transformation of carbon dioxide. *Chem. Rev.* **2007**, 107, 2365–2387.

(15) Chang, X.; Wang, T.; Gong, J. CO_2 photo-reduction: insights into CO_2 activation and reaction on surfaces of photocatalysts. *Energy Environ. Sci.* **2016**, 9, 2177–2196.

(16) Inoue, T.; Fujishima, A.; Konishi, S.; Honda, K. Photoelectrocatalytic reduction of carbon dioxide in aqueous suspensions of semiconductor powders. *Nature* **1979**, 277, 637–638.

(17) Xiong, Z.; Lei, Z.; Li, Y.; Dong, L.; Zhao, Y.; Zhang, J. A review on modification of facet-engineered TiO_2 for photocatalytic CO_2 reduction. *J. Photochem. Photobiol., C* **2018**, 36, 24–47.

(18) Jiang, M.; Huang, K.; Liu, J.; Wang, D.; Wang, Y.; Wang, X.; Li, Z.; Wang, X.; Geng, Z.; Hou, X.; Feng, S. Magnetic-field-regulated TiO_2 {100} facets: a strategy for C–C coupling in CO_2 photocatalytic conversion. *Chem* **2020**, 6, 2335–2346.

(19) Wang, L.; Tan, H.; Zhang, L.; Cheng, B.; Yu, J. In-situ growth of few-layer graphene on ZnO with intimate interfacial contact for enhanced photocatalytic CO_2 reduction activity. *Chem. Eng. J.* **2021**, 411, 128501.

(20) Geng, Z.; Kong, X.; Chen, W.; Su, H.; Liu, Y.; Cai, F.; Wang, G.; Zeng, J. Oxygen vacancies in ZnO nanosheets enhance CO_2 electrochemical reduction to CO. *Angew. Chem. Int. Ed.* **2018**, 57, 6054–6059.

(21) Liang, M.; Borjigin, T.; Zhang, Y.; Liu, B.; Liu, H.; Guo, H. Controlled assemble of hollow heterostructured g-C_3N_4@CeO_2 with rich oxygen vacancies for enhanced photocatalytic CO_2 reduction. *Appl. Catal. B: Environ.* **2019**, 243, 566–575.

(22) Wang, M.; Shen, M.; Jin, X.; Tian, J.; Shao, Y.; Zhang, L.; Li, Y.; Shi, J. Exploring the enhancement effects of hetero-metal doping in CeO_2 on CO_2 photocatalytic reduction performance. *Chem. Eng. J.* **2022**, 427, 130987.

(23) Jiang, Y.; Chen, H.; Li, J.; Liao, J.; Zhang, H.; Wang, X.; Kuang, D. Z-Scheme 2D/2D heterojunction of $CsPbBr_3$/Bi_2WO_6 for improved photocatalytic CO_2 reduction. *Adv. Funct. Mater.* **2020**, 30, 2004293.

(24) Liu, S.; Wang, C.; Wu, J.; Tian, B.; Sun, Y.; Lv, Y.; Mu, Z.; Sun, Y.; Li, X.; Wang, F.; Wang, Y.; Tang, L.; Wang, P.; Li, Y.; Ding, M. Efficient CO_2 electroreduction with a monolayer Bi_2WO_6 through a metallic intermediate surface state. *ACS Catal.* **2021**, 11, 12476–12484.

(25) Yamamoto, M.; Yoshida, T.; Yamamoto, N.; Nomoto, T.; Yamamoto, Y.; Yagi, S.; Yoshida, H. Photocatalytic reduction of CO_2 with water promoted by Ag clusters in Ag/Ga_2O_3 photocatalysts. *J. Mater. Chem. A* **2015**, 3, 16810–16816.

(26) Akatsuka, M.; Kawaguchi, Y.; Itoh, R.; Ozawa, A.; Yamamoto, M.; Tanabe, T.; Yoshida, T. Preparation of Ga_2O_3 photocatalyst highly active for CO_2 reduction with water without cocatalyst. *Appl. Catal. B: Environ.* **2020**, 262, 118247.

(27) Huang, Z.; Teramura, K.; Asakura, H.; Hosokawa, S.; Tanaka, T. CO_2 capture, storage, and conversion using a praseodymium-modified Ga_2O_3 photocatalyst. *J. Mater. Chem. A* **2017**, 5, 19351–19357.

(28) Wang, F.; Hou, T.; Zhao, X.; Yao, W.; Fang, R.; Shen, K.; Li, Y. Ordered macroporous carbonous frameworks implanted with CdS quantum dots for efficient photocatalytic CO_2 reduction. *Adv. Mater.* **2021**, 33, 2102690.

(29) Su, B.; Huang, L.; Xiong, Z.; Yang, Y.; Hou, Y.; Ding, Z.; Wang, S. Branch-like ZnS-DETA/CdS hierarchical heterostructures as an efficient photocatalyst for visible light CO_2 reduction. *J. Mater. Chem. A* **2019**, 7, 26877–26883.

(30) Wang, S.; Guan, B. Y.; Lou, X. W. D. Construction of $ZnIn_2S_4$-In_2O_3 hierarchical tubular heterostructures for efficient CO_2 photoreduction. *J. Am. Chem. Soc.* **2018**, 140, 5037–5040.

(31) Wang, S.; Guan, B. Y.; Wang, X.; Lou, X. W. D. Formation of hierarchical Co_9S_8@$ZnIn_2S_4$ heterostructured cages as an efficient photocatalyst for hydrogen evolution. *J. Am. Chem. Soc.* **2018**, 140, 15145–15148.

(32) He, Y.; Rao, H.; Song, K.; Li, J.; Yu, Y.; Lou, Y.; Li, C.; Han, Y.; Shi, Z.; Feng, S. 3D Hierarchical $ZnIn_2S_4$ nanosheets with rich Zn vacancies boosting photocatalytic CO_2 reduction. *Adv. Funct. Mater.* **2019**, 29, 1905153.

(33) Chen, K.; Wang, X.; Li, Q.; Feng, Y.; Chen, F.; Yu, Y. Spatial distribution of $ZnIn_2S_4$ nanosheets on g-C_3N_4 microtubes promotes photocatalytic CO_2 reduction. *Chem. Eng. J.* **2021**, 418, 129476.

(34) Mao, S.; Shi, J.; Sun, G.; Ma, D.; He, C.; Pu, Z.; Song, K.; Cheng, Y. Au nanodots@thiol-UiO66@$ZnIn_2S_4$ nanosheets with significantly enhanced visible-light photocatalytic H_2 evolution: the effect of different Au positions on the transfer of electron-hole pairs. *Appl. Catal. B: Environ.* **2021**, 282, 119550.

(35) Chen, Y.; Huang, R.; Chen, D.; Wang, Y.; Liu, W.; Li, X.; Li, Z. Exploring the different photocatalytic performance for dye degradations over hexagonal $ZnIn_2S_4$ microspheres and cubic $ZnIn_2S_4$ nanoparticles. *ACS Appl. Mater. Interfaces* **2012**, 4, 2273–2279.

(36) Wang, L.; Cheng, B.; Zhang, L.; Yu, J. In situ irradiated XPS investigation on S-scheme TiO_2@$ZnIn_2S_4$ photocatalyst for efficient photocatalytic CO_2 reduction. *Small* **2021**, 17, 2103447.

(37) Xu, F.; Zhang, L.; Cheng, B.; Yu, J. Direct Z-scheme TiO_2/NiS core-shell hybrid nanofibers with enhanced photocatalytic H_2-production activity. *ACS Sustain. Chem. Eng.* **2018**, 6, 12291–12298.

(38) Chen, B.; Shen, Y.; Wei, J.; Xiong, R.; Shi, J. Research progress on g-C_3N_4-based Z-scheme photocatalytic system. *Acta Phys.-Chim. Sin.* **2016**, 32, 1371–1382.

(39) Yang, X.; Xue, H.; Xu, J.; Huang, X.; Zhang, J.; Tang, Y.; Ng, T. W.; Kwong, H.; Meng, X.; Lee, C. Synthesis of porous ZnS:Ag_2S nanosheets by ion exchange for photocatalytic H_2 generation. *ACS Appl. Mater. Interaces* **2014**, 6, 9078–9084.

(40) Yu, H.; Dong, Q.; Jiao, Z.; Wang, T.; Ma, J.; Lu, G.; Bi, Y. Ion exchange synthesis of PAN/Ag_3PO_4 core-shell nanofibers with enhanced photocatalytic properties. *J. Mater. Chem. A* **2014**, 2, 1668–1671.

(41) Wang, X.; Wang, X.; Huang, J.; Li, S.; Meng, A.; Li, Z. Interfacial chemical bond and internal electric field modulated Z-scheme S_v-$ZnIn_2S_4$/$MoSe_2$ photocatalyst for efficient hydrogen evolution. *Nat. Commun.* **2021**, 12, 4112.

(42) Wang, S.; Zhu, B.; Liu, M.; Zhang, L.; Yu, J.; Zhou, M. Direct Z-scheme ZnO/CdS hierarchical photocatalyst for enhanced photocatalytic H_2-production activity. *Appl. Catal. B: Environ.* **2019**, 243, 19–26.

(43) Li, B.; Wang, W.; Zhao, J.; Wang, Z.; Su, B.; Hou, Y.; Ding, Z.; Ong, W. J.; Wang, S. All-solid-state direct Z-scheme $NiTiO_3$/$Cd_{0.5}Zn_{0.5}S$ heter-

DOI: 10.14102/j.cnki.0254-5861.2021-0026

ostructures for photocatalytic hydrogen evolution with visible light. *J. Mater. Chem. A* **2021**, 9, 10270–10276.

(44) Li, A.; Pang, H.; Li, P.; Zhang, N.; Chen, G.; Meng, X.; Liu, M.; Liu, X.; Ma, R.; Ye, J. Insights into the critical dual-effect of acid treatment on $Zn_xCd_{1-x}S$ for enhanced photocatalytic production of syngas under visible light. *Appl. Catal. B: Environ.* **2021**, 288, 119976.

(45) Zhang, G.; Sun, J.; Chen, D.; Li, N.; Xu, Q.; Li, H.; He, J.; Lu, J. Hierarchical core-shell heterostructures of $ZnIn_2S_4$ nanosheets on electrospun In_2O_3 nanofibers with highly enhanced photocatalytic activity. *J. Hazard. Mater.* **2020**, 398, 122889.

(46) Kuang, P.; Zhang, L.; Cheng, B.; Yu, J. Enhanced charge transfer kinetics of Fe_2O_3/CdS composite nanorod arrays using cobalt-phosphate as cocatalyst. *Appl. Catal. B: Environ.* **2017**, 218, 570–580.

(47) You, Y.; Wang, S.; Xiao, K.; Ma, T.; Zhang, Y.; Huang, H. Z-Scheme g-C_3N_4/Bi_4NbO_8Cl heterojunction for enhanced photocatalytic hydrogen production. *ACS Sustainable Chem. Eng.* **2018**, 6, 16219–16227.

(48) Su, Y.; Ao, D.; Liu, H.; Wang, Y. MOF-derived yolk-shell CdS microcubes with enhanced visible-light photocatalytic activity and stability for hydrogen evolution. *J. Mater. Chem. A* **2017**, 5, 8680–8689.

(49) Zhou, M.; Wang, S.; Yang, P.; Luo, Z.; Yuan, R.; Asiri, A. M.; Wakeel, M.; Wang, X. Layered heterostructures of ultrathin polymeric carbon nitride and $ZnIn_2S_4$ nanosheets for photocatalytic CO_2 reduction. *Chem. Eur. J.* **2018**, 24, 18529–18534.

(50) Li, X.; Jiang, H.; Ma, C.; Zhu, Z.; Song, X.; Li, X.; Wang, H.; Huo, P.; Chen, X. Construction of a multi-interfacial-electron transfer scheme for efficient CO_2 photoreduction: a case study using $CdIn_2S_4$ micro-flower spheres modified with Au nanoparticles and reduced graphene oxide. *J. Mater. Chem. A* **2020**, 8, 18707–18714.

(51) Wang, S.; Yao, W.; Lin, J.; Ding, Z.; Wang, X. Cobalt imidazolate metal-organic frameworks photosplit CO_2 under mild reaction conditions. *Angew. Chem. Int. Ed.* **2014**, 53, 1034–1038.

(52) Lin, X.; Xie, Z.; Su, B.; Zheng, M.; Dai, W.; Hou, Y.; Ding, Z.; Lin, W.; Fang, Y.; Wang, S. Well-defined Co_9S_8 cages enable the separation of photoexcited charges to promote visible-light CO_2 reduction. *Nanoscale* **2021**, DOI: 10.1039/D1031NR04812K.

(53) Zhao, Z.; Shi, C.; Shen, Q.; Li, W.; Men, D.; Xu, B.; Sun, Y.; Li, C. Hierarchical Z-scheme Fe_2O_3@$ZnIn_2S_4$ core-shell heterostructures with enhanced adsorption capacity enabling significantly improved photocatalytic CO_2 reduction. *CrystEngComm* **2020**, 22, 8221–8227.

(54) Zhu, K.; Ou-Yang, J.; Zeng, Q.; Meng, S.; Teng, W.; Song, Y.; Tang, S.; Cui, Y. Fabrication of hierarchical $ZnIn_2S_4$@CNO nanosheets for photocatalytic hydrogen production and CO_2 photoreduction. *Chin. J. Catal.* **2020**, 41, 454–463.

(55) Wang, S.; Guan, B. Y.; Lu, Y.; Lou, X. W. D. Formation of hierarchical In_2S_3-$CdIn_2S_4$ heterostructured nanotubes for efficient and stable visible light CO_2 reduction. *J. Am. Chem. Soc.* **2017**, 139, 17305–17308.

(56) Vu, N. N.; Kaliaguine, S.; Do, T. O. Synthesis of the g-C_3N_4/CdS nanocomposite with a chemically bonded interface for enhanced sunlight-driven CO_2 photoreduction. *ACS Appl. Energy Mater.* **2020**, 3, 6422–6433.

(57) Wang, R.; Yang, P.; Wang, S.; Wang, X. Distorted carbon nitride nanosheets with activated n → π* transition and preferred textural properties for photocatalytic CO_2 reduction. *J. Catal.* **2021**, 402, 166–176.

(58) Wang, S.; Hou, Y.; Wang, X. Development of a stable $MnCo_2O_4$ cocatalyst for photocatalytic CO_2 reduction with visible light. *ACS Appl. Mater. Interfaces* **2015**, 7, 4327–4335.

(59) Niu, P.; Pan, Z.; Wang, S.; Wang, X. Tuning crystallinity and surface hydrophobicity of a cobalt phosphide cocatalyst to boost CO_2 photoreduction performance. *ChemSusChem* **2021**, 14, 1302–1307.

(60) Wang, Y.; Wang, S.; Lou, X. W. Dispersed nickel cobalt oxyphosphide nanoparticles confined in multichannel hollow carbon fibers for photocatalytic CO_2 reduction. *Angew. Chem. Int. Ed.* **2019**, 58, 17236–17240.

(61) Yang, M.; Xu, Y.; Lu, W.; Zeng, K.; Zhu, H.; Xu, Q.; Ho, G. W. Self-surface charge exfoliation and electrostatically coordinated 2D hetero-layered hybrids. *Nat. Commun.* **2017**, 8, 14224.

(62) Xu, J.; Sun, C.; Wang, Z.; Hou, Y.; Ding, Z.; Wang, S. Perovskite oxide $LaNiO_3$ nanoparticles for boosting H_2 evolution over commercial CdS with visible light. *Chem. Eur. J.* **2018**, 24, 18512–18517.

(63) He, F.; Zhu, B.; Cheng, B.; Yu, J.; Ho, W.; Macyk, W. 2D/2D/0D TiO_2/C_3N_4/Ti_3C_2 MXene composite S-scheme photocatalyst with enhanced CO_2 reduction activity. *Appl. Catal. B: Environ.* **2020**, 272, 119006.

(64) Wu, Y.; Xie, N.; Li, X.; Fu, Z.; Wu, X.; Zhu, Q. MOF-derived hierarchical hollow NiRu-C nanohybrid for efficient hydrogen evolution reaction. *Chin. J. Struct. Chem.* **2021**, 40, 1346–1356.

(65) Xiong, Z.; Huang, L.; Peng, J.; Hou, Y.; Ding, Z.; Wang, S. Spinel-type mixed metal sulfide $NiCo_2S_4$ for efficient photocatalytic reduction of CO_2 with visible light. *ChemCatChem* **2019**, 11, 5513–5518.

(66) Deng, H.; Fei, X.; Yang, Y.; Fan, J.; Yu, J.; Cheng, B.; Zhang, L. S-scheme heterojunction based on p-type $ZnMn_2O_4$ and n-type ZnO with improved photocatalytic CO_2 reduction activity. *Chem. Eng. J.* **2021**, 409, 127377.

(67) Mahadadalkar, M. A.; Gosavi, S. W.; Kale, B. B. Interstitial charge transfer pathways in a TiO_2/$CdIn_2S_4$ heterojunction photocatalyst for direct conversion of sunlight into fuel. *J. Mater. Chem. A* **2018**, 6, 16064–16073.

(68) Zuo, G.; Wang, Y.; Teo, W. L.; Xian, Q.; Zhao, Y. Direct Z-scheme TiO_2-$ZnIn_2S_4$ nanoflowers for cocatalyst-free photocatalytic water splitting. *Appl. Catal. B: Environ.* **2021**, 291, 120126.

(69) Tang, S.; Yin, X.; Wang, G.; Lu, X.; Lu, T. Single titanium-oxide species implanted in 2D g-C_3N_4 matrix as a highly efficient visible-light CO_2 reduction photocatalyst. *Nano Res.* **2019**, 12, 457–462.

Received: November 4, 2021
Accepted: December 1, 2021
Published: January 13, 2022

DOI: 10.14102/j.cnki.0254-5861.2021-0026